The Astrophysical Journal, 649:541–552, 2006 September 20

SWIFT X-RAY TELESCOPE OBSERVATIONS OF THE *DEEP IMPACT* COLLISION

R. Willingale,[1] P. T. O'Brien,[1] S. W. H. Cowley,[1] G. H. Jones,[2] D. J. McComas,[3] K. O. Mason,[4] J. P. Osborne,[1] A. Wells,[1] M. Chester,[5] S. Hunsberger,[5] D. N. Burrows,[5] N. Gehrels,[6] J. A. Nousek,[5] L. Angelini,[6,7] L. R. Cominsky,[8] S. L. Snowden,[6] and G. Chincarini[9]

Received 2006 March 7; accepted 2006 May 29

ABSTRACT

Comet 9P/Tempel 1 was observed by the *Swift* X-Ray Telescope (XRT) for a total of 250,024 s. Soft X-ray emission, 0.2–1.0 keV, was seen as a diffuse extended halo with an FWHM of 1.03×10^5 km centered on the comet's nucleus. The X-ray light curve indicates that the comet exhibited a prolonged soft X-ray outburst just after impact of the NASA *Deep Impact* (*DI*) spacecraft and enhanced X-ray activity lasted for 12 days. The radial brightness distribution and X-ray spectrum are in excellent agreement with a model of X-ray production in which highly charged minor heavy ion species in the solar wind undergo charge exchange reactions with water group or carbon dioxide group molecules in the neutral coma of the comet. Using this model, we derive a simple expression for the X-ray emission and show that the X-ray flare is, in part, due to an increase in solar wind flux at the comet but is largely due to an enhanced molecule production rate. Assuming that the main outgassing constituent was water, the comet produced $(2.9 \pm 0.4) \times 10^8$ kg over the 12 day period postimpact. The quiescent water production was expected to inject $\sim 1.0 \times 10^8$ kg into the coma over the same period so the observed X-ray flux indicates that an additional $(1.9 \pm 0.4) \times 10^8$ kg of water or, alternatively, $(3.9 \pm 0.5) \times 10^8$ kg of carbon dioxide were liberated by the *DI* impact.

Subject headings: comets: general — comets: individual (9P/Tempel 1)

Online material: color figures

1. INTRODUCTION

On 2005 July 4 at about 05:44:36 UT a spacecraft of mass 364 kg (plus 6.5 kg of unused fuel) released from the NASA *Deep Impact* (*DI*) mission hit the surface of comet 9P/Tempel 1. The impact speed was 10.3 km s^{-1}, and *DI* delivered 19 GJ of kinetic energy to the nucleus of the comet (A'Hearn et al. 2005). The event was witnessed by Medium and High Resolution Instruments (MRI and HRI) on the flyby spacecraft from a distance of ~500 km and by many ground-based and space-based telescopes (Earth-received time of impact 05:52:02 UT; Meech et al. 2005).

Following an initial optical flash at impact, a fast plume of material was observed moving outward from the impact site at a projected velocity of 5 km s^{-1}. The true velocity of this material is likely to have been 7–10 km s^{-1} depending on the angle with respect to the surface (A'Hearn et al. 2005). Using scaling relationships derived from laboratory measurements of gravity-dominated cratering, the gravity field local to the impact site can be used to derive an estimate of the total mass for the comet nucleus $7.2^{+4.8}_{-3.8} \times 10^{13}$ kg and a bulk density of 400 ± 300 kg m^{-3} (Richardson & Melosh 2006[10]). Preliminary conclusions from the ground- and space-based campaign were that the material shed by the comet after impact was compositionally different from that seen before impact and that the dust-to-gas ratio was larger after impact. However, the enhanced activity seen after impact did not last for more than 5 days, by which time the behavior of the comet was indistinguishable from the preimpact behavior (Meech et al. 2005). Gas species CN, C_2, C_3, NH_2, and CH monitored in visible spectra increased in intensity by a factor of ~1.5–5 during 1–2 days after impact, but by July 9 they dropped to preimpact levels. During the first 20 hr the leading edge of the dust cloud was expanding at $\sim 200 \pm 20$ m s^{-1} and, assuming a typical albedo, the total mass of dust ejected was $\sim 10^6$ kg (Meech et al. 2005).

The OSIRIS camera system on the ESA *Rosetta* spacecraft observed the comet before and after impact (Küppers et al. 2005). Emission of OH at 308 nm was used to derive the water production rate preimpact. Assuming an outflow velocity of 0.7 km s^{-1} typical for a distance of 1.5 AU from the Sun, the rate was $(3.4 \pm 0.5) \times 10^{27}$ molecules s^{-1}. If the outflow was 1 km s^{-1}, then the production rate was $(5.8 \pm 1.0) \times 10^{27}$ molecules s^{-1}, which is in good agreement with near-ultraviolet measurements (Schleicher & Barnes 2005; Schleicher et al. 2006). Using the Wide Angle Camera (WAC) images at 308 nm postimpact, Küppers et al. (2005) estimate that the total amount of water released by the impact was $(1.5 \pm 0.5) \times 10^{32}$ molecules or 4.6×10^6 kg, which is only ~20% of the daily production rate at preimpact levels. The beam size used for the analysis had a radius equivalent to 1.56×10^5 km centered on the position of the comet nucleus, and the number of OH molecules was measured over the period −20 to +30 hr with respect to the impact. The Narrow Angle Camera (NAC) images taken at 648 nm (orange filter) show a

[1] Department of Physics and Astronomy, University of Leicester, University Road, Leicester LE1 7RH, UK.
[2] Max-Planck-Institut für Sonnensystemforschung, Max-Planck-Strasse 2, 37191 Katlenburg-Lindau, Germany.
[3] Southwest Research Institute, PO Drawer 28510, San Antonio, TX 78228.
[4] Mullard Space Science Laboratory, University College London, Holmbury St. Mary, Dorking RH5 6NT, UK.
[5] Department of Astronomy and Astrophysics, Pennsylvania State University, 525 Davey Laboratory, University Park, PA 16802.
[6] NASA Goddard Space Flight Center, Greenbelt, MD 20771.
[7] Universities Space Research Association, 10211 Wincopin Circle, Suite 500, Columbia, MD 21033-3432.
[8] Department of Physics and Astronomy, Sonoma State University, Rohnert Park, CA 94928.
[9] Istituto Nazionale di Astrofisica, Osservatorio Astronomico di Brera, Via E. Bianchi 46, I-23807 Merate (LC), Italy.

[10] See http://www.lpi.usra.edu/meetings/lpsc2006/pdf/1836.pdf.

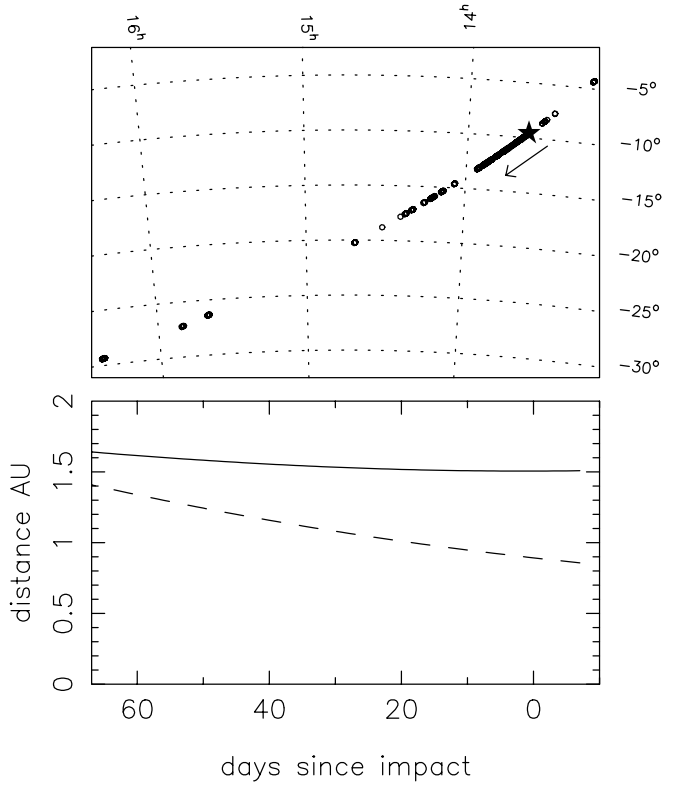

FIG. 1.—Ephemeris of 9P/Tempel 1. *Top: Swift* observations of 9P/Tempel 1 plotted in right ascension and declination. The circles represent the size of the field of view of the XRT. The black star indicates the position of impact, and the arrow shows the direction of travel across the sky. *Bottom:* Distance of the comet from the Sun (*solid line*) and the range of the comet from Earth (*dashed line*). Note that time runs from right to left. [*See the electronic edition of the Journal for a color version of this figure.*]

core of emission of diameter $\sim 2 \times 10^4$ km with a peak brightness ~20 hr after impact.

2. *SWIFT* OBSERVATIONS

The *Swift* X-Ray Telescope (XRT; Gehrels et al. 2004; Burrows et al. 2005) observed 9P/Tempel 1 for a total exposure time of 250,024 s over a period starting 13 days before the impact through to 65 days after. Figure 1 shows the pointings along the track of the comet during this period. The circles represent the field of view of the XRT pre- and postimpact. The black star indicates the position of the comet at impact. The bottom panel gives the distance to the comet and distance of the comet from the Sun over the same period. A total exposure of 197,683 s was concentrated into the 20 days immediately after impact. The on-time is broken up into time slots of typically a few thousand seconds with gaps of a similar duration because of the viewing constraints of the satellite. The point-spread function (PSF) of the XRT has a half-energy width of ~18″, corresponding to $\sim 2.4 \times 10^4$ km at the distance of the comet, 1.0 AU. The field of view is ~23′ in diameter and the energy band is 0.2–10 keV.

3. DATA ANALYSIS

All of the *Swift* exposures were made using a fixed pointing in right ascension and declination, so the X-ray events had to be repositioned into a coordinate system centered on the position of the comet during each exposure using the ephemeris compiled by the Solar System Dynamics Group at JPL.[11] The diffuse background level and background spectrum were estimated using an annulus of radius 5′–8′ centered on the comet position. Figure 2 shows the background-subtracted X-ray light curve 0.2–1.0 keV for a beam of radius 2′ centered on the position of the comet. Each data point represents approximately 20,000 s of exposure. We tried producing an X-ray light curve with higher time resolution, but the count rate from the comet was too small to provide adequate statistics. Because the comet is moving across the sky, it is possible that point X-ray sources moved through the central beam or the background annulus during the exposures. We screened every exposure to check for this. Several such sources were found and some exposures were truncated to avoid contamination of the comet signal.

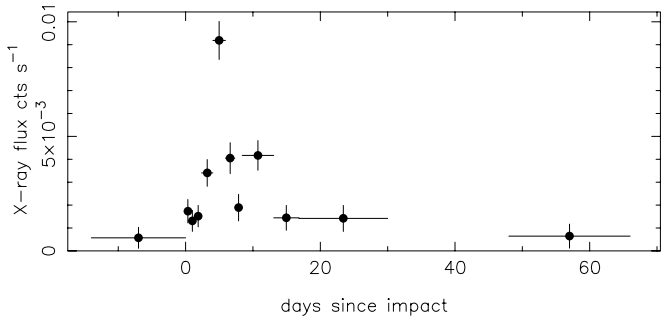

FIG. 2.—Soft X-ray light curve 0.2–1.5 keV. Each data point corresponds to ~20,000 s of exposure. $T = 0$ on this and subsequent plots corresponds to impact as seen from the *Swift* satellite.

Figure 3 is a background-subtracted image of the comet accumulated over the period 0–20 days after impact. The right panel shows the radial surface brightness distribution. The solid line is a "Moffatt" profile of the form

$$f(r) = f_0 \left[1 + (r/r_c)^2\right]^{-1/2}, \quad (1)$$

where r_c is a core radius. For $r \gg r_c$, $f(r) \sim 1/r$, while for $r \leq r_c$, the profile is rounded off such that the gradient vanishes at $r = 0$. The best-fit profile gave $r_c = 13''$ (consistent with the width of the core of the PSF [FWHM 7″, half-energy width 18″] and equivalent to 1.7×10^4 km at the comet). There is no significant asymmetry in the brightness distribution. (The fact that the bright pixels spell "T" for 9P/Tempel 1 is a statistical accident caused by the binning!) The centroid of the distribution is 11″ (equivalent to 1.4×10^4 km at the comet) from the position of the optical core, but this offset is insignificant given the counting statistics and the width of the distribution, FWHM 78″ (1.03×10^5 km at the comet).

Figure 4 shows the soft X-ray spectrum of the comet accumulated in the same beam as the X-ray light curve, again for the period 0–20 days after impact. The spectrum was fitted using XSPEC (Arnaud 1996) assuming that the X-ray emission arises solely from lines. Individual lines were included one after the other until all of the major "peaks" were modeled. With seven lines $\chi^2 = 81.6$ with 45 degrees of freedom. Although the reduced χ^2, $\chi^2_\nu = 1.8$, was rather large, there were no obvious features that could be modeled by the addition of an extra line. Table 1 gives a list of the line energies and line strengths. The strengths of individual lines are very poorly determined because of the limited statistics in the spectrum, but the overall flux is reasonably well constrained. The mean count rate was $(7.7 \pm 0.2) \times 10^{-3}$ m^{-2} s^{-1} and the corresponding flux $(1.75 \pm 0.05) \times 10^{-16}$ J m^{-2} s^{-1} in the energy band 0.2–1.0 keV. The mean energy of the incident

[11] See http://ssd.jpl.nasa.gov.

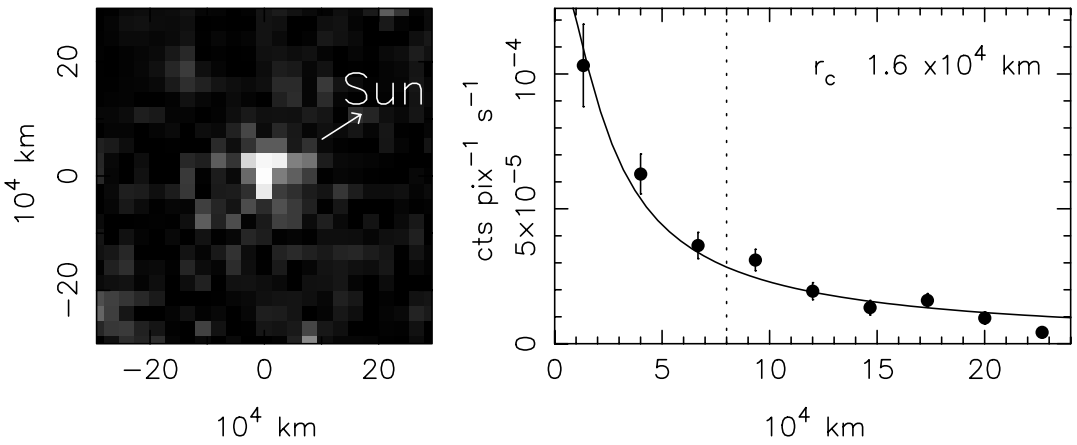

FIG. 3.—*Left:* X-ray image of the comet for 0–20 days since impact. The pixel size is 40″, equivalent to $\approx 2.7 \times 10^4$ km at the comet. *Right:* X-ray surface brightness of the comet. The vertical dotted line indicates the radius of the beam used to produce the X-ray light curve. [*See the electronic edition of the Journal for a color version of this figure.*]

spectrum is 0.46 keV although this may be biased by the low-energy cutoff of the *Swift* XRT, 0.2 keV.

4. SIMPLE THEORETICAL MODEL OF X-RAY POWER OUTPUT

Cometary X-rays are produced when highly charged minor heavy ion species in the solar wind undergo charge exchange reactions with water group molecules in the cometary neutral coma (Cravens 1997, 2002; Häberli et al. 1997; Krasnopolsky 1997; Wegmann et al. 1998). The observed spectrum of 9P/Tempel 1 shown in Figure 4 is consistent with the emission expected from this mechanism. The part-neutralized solar wind ions are formed in highly excited states, which then decay with the emission of X-ray photons. Possible identifications of the solar wind ions are given at the top of Figure 4 and in Table 1. For example, O^{+8} ions in the solar wind can exchange charge with neutral species N^0 ($N^0 = H_2O$, OH, . . .) to produce excited O^{+7*} ions, $O^{+8} + N^0 \rightarrow O^{+7*} + N^{+1}$. The excited O^{+7*} ion then emits a photon, usually designated O VIII.

In this section we derive a theoretical model of cometary X-ray power output based on this picture, which allows simple estimates to be made of the molecular production rate from the *Swift* data.

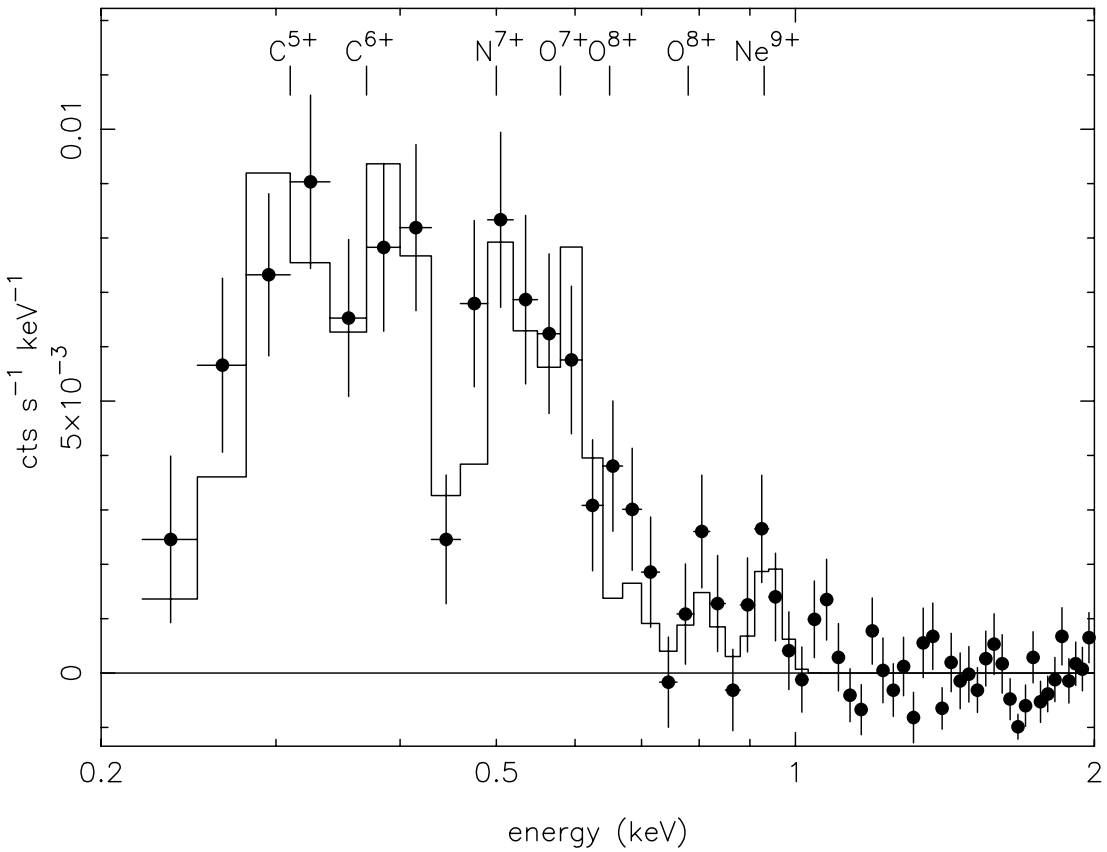

FIG. 4.—Soft X-ray spectrum of 9P/Tempel 1. The line energies marked correspond to the approximate positions predicted for charge exchange between the solar wind ions indicated and neutral gas in the comet's coma. The histogram is the best-fit model, which comprises seven emission lines.

TABLE 1
Emission Lines in the Spectral Fit

Line Energy (keV)	Line Strength (10^{-5} photons cm^{-2} s^{-1})	Ion
0.31 ± 0.15	1.37	C^{+5}
0.38 ± 0.05	3.70	C^{+6}
0.50 ± 0.20	0.99	N^{+7}
0.58 ± 0.05	1.76	O^{+7}
0.66 ± 0.08	0.40	O^{+8}
0.79 ± 0.07	0.22	O^{+8}
0.93 ± 0.02	0.21	Ne^{+9}

Note.—The last column shows possible source ions in the solar wind.

The details of the calculation, specifically the nature of the approximations that can be made, depend on the beam size used to collect the X-ray photons relative to the size of the comet's neutral coma and the plasma structures that result from the solar wind interaction, as discussed below. Here we focus on the *Swift* measurements in Figure 2, which show the X-ray flux emitted from a region within 2′ of the nucleus as observed from the *Swift* orbit. At the time of impact of the *DI* spacecraft the Earth-comet distance was ~0.89 AU (see Fig. 1, *bottom panel*), such that this region then corresponded to a radial distance of $\sim 7.8 \times 10^4$ km from the nucleus. Since the Earth-comet distance slowly increased during the period of observations (again, see Fig. 1), however, so did the radius of the corresponding region surrounding the nucleus, from $\sim 6 \times 10^4$ km at the beginning of the interval to $\sim 1.2 \times 10^5$ km toward its end (see also §§ 5 and 6).

The X-ray radiated power per unit volume in the cometary coma can be written as

$$p_{\rm X} = E_{\rm CE}\sigma\alpha n_p \nu_p n_n, \tag{2}$$

where $E_{\rm CE} \approx 250$ eV is the average X-ray energy output per heavy ion that undergoes charge exchange, $\sigma \approx 3 \times 10^{-19}$ m^2 is the charge exchange cross section, $\alpha \approx 10^{-3}$ is the fractional abundance of heavy ions in the solar wind, n_p is the number density of solar wind protons, ν_p is their speed, and n_n is the number density of neutral molecules in the cometary coma (see, e.g., the parameter values given by Schwadron & Cravens 2000; Wegmann et al. 2004). The charge exchange parameters given above represent typical values employed for a "target" coma dominated by water molecules and their photodissociation products (OH, O, and H), as is generally the case for periodic comets such as 9P/Tempel 1. It seems possible, however, that the *DI* collision may also have led to the release of significant amounts of carbon dioxide from the interior of the nucleus. However, since the ionization potential for carbon dioxide (13.8 eV) is almost the same as for water and its dissociation products (13.6 eV for O, 13.8 eV for OH, 12.6 eV for H_2O, and 13.6 eV for H), the charge exchange cross sections should be very similar for these gases, as should the average X-ray energy per reaction (e.g., Wegmann et al. 1998). In equation (2) we may thus consider n_n to be the total neutral number density, irrespective of whether the source gas is water, carbon dioxide, or some combination of the two. Water and carbon dioxide molecules are thus considered to be produced by the comet at a combined rate Q and to flow radially outward with speed $\nu_n \approx 1$ km s^{-1}. Both species and their photodissociation products are then photoionized by solar radiation on a timescale of $\tau_i \approx 10^6$ s (e.g., Huebner et al. 1992), following which they are "picked up" by the solar wind plasma flow and transported rapidly antisunward. The outward flux of neutral atoms and molecules in the coma thus starts to become significantly depleted by photoionization at distances from the comet of $\sim 10^6$ km. Since this distance is much larger than those of relevance to the *Swift* observations, we can simply take the cometary neutral number density to be given by

$$n_n(r) = \frac{Q}{4\pi\nu_n r^2}, \tag{3}$$

where r is the radial distance from the comet nucleus. This formula assumes a constant molecule production rate. If the production rate changes, then the time required to repopulate the coma within the region inside 2′ from the nucleus is ~1 day with the above neutral particle outflow speed. Note that equations (2) and (3) assume that neither the cometary neutrals nor the solar wind heavy ions are significantly depleted by the charge exchange interaction. This is certainly valid for the cometary neutrals, whose ionization timescale due to charge exchange is more than 1000 times longer than for solar radiation. Below it is also shown to be valid for the solar wind heavy ions under the conditions at 9P/Tempel 1, throughout most of the region surrounding the nucleus sampled by *Swift*.

We first assume that the solar wind flows unmodified through the cometary coma, such that n_p and ν_p in equation (2) are the upstream solar wind proton density and speed, respectively. Below we consider the modifications that result from solar wind mass loading by cometary ions. We thus introduce equation (3) into equation (2) and integrate first along the line of sight for a given "impact parameter" r' relative to the nucleus, to find the X-ray power per unit area

$$P'_{\rm X1} = \frac{E_{\rm CE}\sigma\alpha F_p Q}{4\nu_n r'}, \tag{4}$$

where $F_p = n_p\nu_p$ is the proton flux in the solar wind. Equation (4) is valid for values of r' less than $\sim 10^6$ km, within which distance equation (2) is valid. The emitted power per unit area within this distance should thus vary inversely with the radial distance from the nucleus, in agreement with the results shown in Figure 3. We then integrate equation (4) over the area from the nucleus to radial distance R to find the total X-ray power emitted within radius R to be given by

$$P_{\rm X1} = \frac{\pi E_{\rm CE}\sigma\alpha F_p Q R}{2\nu_n}, \tag{5}$$

whose validity is again limited to distance R smaller than $\sim 10^6$ km. Substituting the above parameter values then yields an X-ray output in megawatts of

$$P_{\rm X1} \approx 18.9 F_p^* Q^* R^*, \tag{6}$$

where F_p^* is the solar wind proton flux in units of 10^{12} m^{-2} s^{-1}, Q^* is the cometary molecule production rate in units of 10^{28} s^{-1}, and R^* is the radial distance from the nucleus in units of 10^5 km.

Within this approximation we can also determine the depletion of high charge state heavy solar wind ions due to charge exchange, as mentioned above. As indicated by equation (2), the rate at which such heavy ions undergo charge exchange with cometary neutrals is given by

$$\frac{dn_h}{dt} = -\left(\sigma\nu_p n_n\right) n_h, \tag{7}$$

where n_h is the number density of solar wind heavy ions, which flow through the coma with the same speed as the solar wind protons. Integrating this expression along a solar wind streamline through the whole coma then yields a depletion relative to the upstream density n_{h0} given by

$$\frac{n_h}{n_{h0}} = \exp\left(-\frac{\sigma Q}{4\nu_n \rho}\right), \tag{8}$$

where ρ is the impact parameter of the solar wind streamline relative to the nucleus. Depletion is thus important only on streamlines that pass within a certain distance of the nucleus, such that the argument of the exponential is of order unity or larger. Setting the argument to be equal to 1, we have a limiting radial distance of

$$\rho_{\rm lim} = \frac{\sigma Q}{4\nu_n} \approx 750 Q^* \text{ km}. \tag{9}$$

Thus, the region within which heavy ion depletion is significant becomes comparable to the size of the region observed by *Swift* ($\sim 10^5$ km), thereby invalidating the above analysis, only for very active comets with $Q^* \geq 100$ (i.e., $Q \geq 10^{30}$ s^{-1}). For relatively weak comets such as 9P/Tempel 1 with $Q^* \sim 1$ at perihelion (Belton et al. 2005), $\rho_{\rm lim}$ is 2 orders of magnitude smaller than the radius of the region observed. In this case the effect of heavy ion depletion can be ignored throughout most of the interaction region, except for the tiny volume of streamlines that pass very close to the nucleus. This situation corresponds to the "collisionally thin" case recently discussed for comet 2P/Encke (also with $Q^* \sim 1$ at perihelion) by Lisse et al. (2005).

We now consider the modifications of equations (5) and (6) that are introduced by the interaction between the solar wind and the cometary coma gas. First, in the vicinity of the comet the solar wind is slowed by the pickup of heavy ions from the coma that are produced (predominantly) by photoionization of the neutral molecules by solar radiation. This leads to the formation of a shock or bow wave upstream of the nucleus, downstream of which the plasma density is significantly increased, leading to enhanced X-ray production (e.g., Wegmann et al. 2004; Wegmann & Dennerl 2005). Second, the force exerted by the weakly ionized cometary gas close to the nucleus is sufficient to exclude the mass-loaded solar wind plasma and embedded magnetic field from a cavity surrounding the nucleus, such that the X-ray production from this inner region is zero. However, the size of this field-free cavity for comets with $Q^* \sim 1$ is likely to be just a few hundred kilometers (e.g., Cravens & Gombosi 2004), which is too small to significantly affect the results derived here. This second effect will therefore be ignored.

Considering, then, the effect of cometary ion mass loading, we first estimate the radial distance of the shock wave on the comet-Sun line upstream of the comet. If we consider some particular solar wind stream tube, then the flux of singly ionized cometary heavy ions at some position on the tube is equal to the total cometary ion production in the tube upstream from that position, assuming for simplicity that the cometary ions move exactly with the solar wind flow along the stream tube. The cometary ion production rate per unit volume is just n_n/τ_i, where n_n is the cometary neutral number density given by equation (3) (for $r < 10^6$ km) and $\tau_i \approx 10^6$ s is the photoionization time constant for solar radiation introduced above. Integrating this expression on the streamline along the comet-Sun line then yields the cometary ion flux at distance r upstream from the comet (for $r < 10^6$ km) as

$$F_{\rm ci} = n_{\rm ci}\nu_p' = \frac{Q}{4\pi\nu_n\tau_i r}, \tag{10}$$

where ν_p' is the solar wind speed as modified by mass loading. The condition for formation of a shock is that the mass density of the cometary ions should reach a fraction $f \approx 0.3$ of the solar wind mass density (e.g., Galeev et al. 1985). For equal flow speeds, as assumed, we thus require $F_{\rm ci} = (m_p/m_{\rm ci}) f F_p$, where $(m_p/m_{\rm ci})$ is the ratio of the proton to cometary ion mass and F_p is the flux of solar wind protons that is conserved along the stream tube as the flow speed modestly declines due to mass loading upstream of the shock. For a coma that consists of a mixture of water and carbon dioxide molecules and their photodissociation products, we can use the mean particle mass for $m_{\rm ci}$ in approximate calculations, given that the photoionization times τ_i for each of these species are roughly the same within a factor of $\sim$2. The subsolar radial distance of the shock $R_{\rm ss}$ is thus given by

$$R_{\rm ss} = \frac{(m_{\rm ci}/m_p)Q}{4\pi f \nu_n \tau_i F_p} \text{ km}, \tag{11}$$

which we again note is valid only when $R_{\rm ss} < 10^6$ km, and thus not for very active comets, where equation (11) overestimates the shock distance. If we consider the usual water-dominated coma of periodic comets, then the mass ratio $(m_p/m_{\rm ci})$ for water group ions, principally O^+, OH^+, and H_2O^+, can be taken equal to 17. The corresponding subsolar shock distance $R_{\rm ss}$ in km is then given by

$$R_{\rm ss} \approx 4.5 \times 10^4 \frac{Q^*}{F_p^*}. \tag{12}$$

For a pure carbon dioxide coma, however, the mass ratio is 44, noting that CO_2 is photodissociated to CO and O on longer timescales ($\sim 10^6$ s), and thus at larger distances ($\sim 10^6$ km), than H_2O, which is photodissociated to OH and O ($\sim 10^5$ s and hence $\sim 10^5$ km, respectively). For a carbon dioxide–dominated coma the subsolar shock distance $R_{\rm ss}$ is thus given in km by

$$R_{\rm ss} \approx 11.7 \times 10^4 \frac{Q^*}{F_p^*}, \tag{13}$$

which is thus rather larger for a given production rate than for water. As indicated above, equations (12) and (13) are valid for production rates Q^* that are sufficiently small that $R_{\rm ss} < 10^6$ km and thus for relatively weak periodic comets that under usual circumstances are water dominated. For a mixture of the two gases, $R_{\rm ss}$ will lie between these two values in rough proportion to the composition involved. For example, taking $Q^* \approx 3$ and $F_p^* \approx 2$, appropriate to comets 21P/Giacobini-Zinner and 19P/Borrelly at heliocentric distances of $\sim$1 AU, we find $R_{\rm ss} \approx 7 \times 10^4$ km, which is in reasonable accord with observations by the *International Cometary Explorer* (*ICE*) and *Deep Space 1* spacecraft, respectively, when allowance is made for the off-axis locations of the shock observations (see, e.g., the review by Cravens & Gombosi 2004, their Table 1). For 26P/Grigg-Skjellerup with $Q^* \approx 0.75$ we find $R_{\rm ss} \approx 2 \times 10^4$ km, which again appears reasonable in comparison with related *Giotto* observations.

Downstream from the cometary shock the solar wind becomes slowed and compressed, with densities increasing to ~3 times the upstream value in the subsolar sheath region, before falling again as the plasma expands into the downstream flow. For simple calculations, therefore, we assume an additional solar wind density, over and above the upstream value already included in equations (5) and (6), of $\sim 2n_p$ within a sunward-facing hemisphere of radius R_{ss}. The ion speed in equation (2) within this region is still taken as the upstream solar wind speed ν_p, however, but now manifest mainly as ion thermal motions rather than as bulk velocity. The additional solar wind flux within this hemispheric region is thus taken to be $\sim 2F_p$. Integrating equation (2) along the line of sight through this hemisphere and then over the area to radius R from the nucleus yields a total X-ray power (independent of viewing direction), additional to that given in equation (5), of

$$P_{X2} = \frac{E_{CE}\sigma\alpha F_p Q R_{ss}}{\nu_n} g\left(\frac{R}{R_{ss}}\right), \quad (14)$$

where the geometric factor g varies from zero when $R = 0$ to unity when $R \geq R_{ss}$, such that the field of view then contains the whole of the shocked solar wind region. Specifically, for $R \leq R_{ss}$ function g is given by

$$g\left(\frac{R}{R_{ss}}\right) = \left(\frac{R}{R_{ss}}\right)\cos^{-1}\left(\frac{R}{R_{ss}}\right) + 1 - \sqrt{1 - \left(\frac{R}{R_{ss}}\right)^2}. \quad (15)$$

If we now introduce R_{ss} from equation (11) into equation (14), we find

$$P_{X2} = \frac{(m_{ci}/m_p)E_{CE}\sigma\alpha Q^2}{4\pi f \nu_n^2 \tau_i} g\left(\frac{R}{R_{ss}}\right), \quad (16)$$

where the expression multiplying factor g is now independent of the upstream solar wind proton flux F_p because the radius of the region of the enhanced solar wind ion density given by equation (11) is inversely proportional to this flux. Substituting the numbers given above into equation (16), we then find the additional X-ray power due to solar wind mass loading and shock formation for a water-dominated coma to be

$$P_{X2} \approx 5.4 Q^{*2} g \text{ MW}, \quad (17)$$

where (R/R_{ss}) in the g function equation (15) is given by

$$\frac{R}{R_{ss}} \approx 2.2 \frac{F_p^* R^*}{Q^*} \quad (18)$$

from equation (11). In the opposite limit of a carbon dioxide–dominated coma these equations become

$$P_{X2} \approx 14.0 Q^{*2} g \text{ MW} \quad (19)$$

and

$$\frac{R}{R_{ss}} \approx 0.86 \frac{F_p^* R^*}{Q^*}. \quad (20)$$

Finally, then, combining equations (6) and (17) yields the following estimate for the 9P/Tempel 1 X-ray power observed by *Swift* in the usual case of a water-dominated coma:

$$P_X \approx 18.9 F_p^* Q^* R^* + 5.4 Q^{*2} g \text{ MW}, \quad (21)$$

where factor g is given by equations (15) and (18). In the carbon dioxide–dominated limit this becomes

$$P_X \approx 18.9 F_p^* Q^* R^* + 14.0 Q^{*2} g \text{ MW}, \quad (22)$$

where the factor g is given by equations (15) and (20). For intermediate cases of a water–carbon dioxide mixture, the X-ray output may be estimated by combining equations (21) and (22) in the appropriate fractions, with the g factor calculated using equation (15) and R_{ss} determined from the corresponding fractions of equations (12) and (13).

In order to validate the results, it is useful to test our formulation against X-ray power outputs observed for other comets, although only water-dominated periodic comets have been investigated to date. In the original observations of comet Hyakutake by the *Röntgensatellit* (*ROSAT*) spacecraft, for example, the X-ray power in a region $\sim 1.2 \times 10^5$ km surrounding the nucleus was deduced to be ~400 MW (Lisse et al. 1996; Wegmann et al. 1998). With $Q^* \approx 8$ and $F^* \approx 2$ for an assumed typical solar wind at ~1 AU (e.g., a proton density of ~5 cm^{-3} and a solar wind speed of ~400 km s^{-1}), we then find that the region of observations did not extend to the shock vicinity at a radial distance of $\sim 1.8 \times 10^5$ km according to equation (11). We thus have $(R/R_{ss}) \approx \frac{2}{3}$ in this case, such that $g \approx 0.81$, thus giving an estimated power of ~640 MW. This is considered to be in reasonable agreement with the power deduced from *ROSAT* data, given the uncertainty in the value of the solar wind proton flux. We also note that the X-ray power determined from equation (6) (~360 MW), which represents an essentially symmetrical emission about the nucleus varying inversely with the impact parameter relative to the nucleus, and the additional power given by equation (17) associated with the shocked solar wind on the sunward side of the nucleus (~280 MW) are roughly comparable in this case. There should thus be a significant asymmetry in the X-ray emission from the comet in this case, favoring the sunward side, in agreement with observations (Lisse et al. 1996; Wegmann et al. 1998).

More directly germane to the 9P/Tempel 1 regime are the observations of comet 2P/Encke 2003 by the *Chandra* spacecraft, reported by Lisse et al. (2005). In this case ~30 MW of X-ray emission was observed from the region within $\sim 4 \times 10^4$ km of the nucleus, whose production rate is estimated to have been $Q^* \approx 1$. The solar wind flux was estimated to be $F^* \approx 2$, within an uncertainty of ~50%. For these parameters the shock distance from equation (12) is estimated to be $\sim 1.6 \times 10^4$ km, which thus lies within the region of observations, so that $g = 1$. Equation (21) then yields an estimated X-ray power of ~21 MW, which again represents reasonable agreement given the uncertainties involved. The emission associated with the shocked solar wind region given by the second term in equation (21) is a modest fraction (about one-quarter) of the overall emission. Thus, the enhancement of the X-ray flux on the sunward side will be modest in this case, which is also in agreement with the *Chandra* observations presented by Lisse et al. (2005).

Overall, these results provide some confidence that equation (21) forms a reasonable basis on which to interpret the *Swift* observations of 9P/Tempel 1 if the coma is indeed water dominated. In this case the comet was located close to perihelion at ~1.51 AU (see Fig. 1), such that the solar wind flux will be reduced by a factor of ~2 compared with that near the Earth's orbit. Thus, $F^* \approx 1$ may be more typical. Then also putting $R^* \approx 1$ and $g \approx 1$, equation (21) predicts an X-ray power output that increases from ~10 MW for $Q^* \approx 0.5$, to ~25 MW for

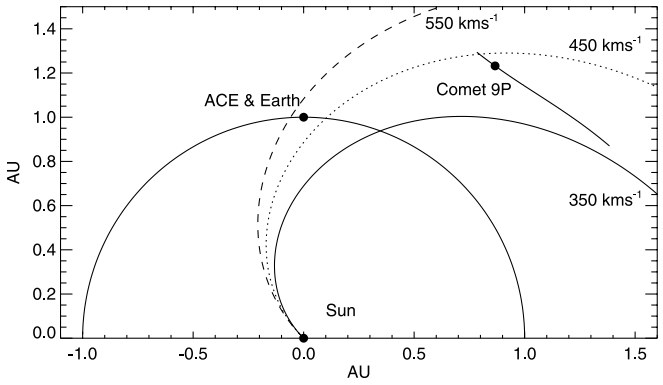

FIG. 5.—Relative positions of Earth, the Sun, and the comet, with respect to a fixed Sun-Earth line, projected onto the ecliptic plane viewed from the north ecliptic pole. Impact occurred at the point on the comet track marked by a filled circle. In this view, the Sun rotates anticlockwise, and the track of material emanating from a single source region on the Sun is plotted for three constant solar wind velocities of 350, 450, and 550 km s^{-1}.

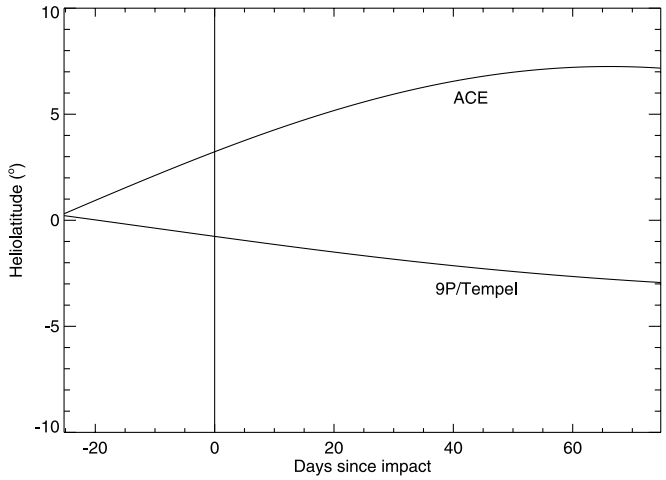

FIG. 7.—Difference in heliographic latitude between *ACE* and 9P/Tempel 1 as a function of time since impact.

$Q^* \approx 1$, and to ~40 MW for $Q^* \approx 1.5$. For the same production rates of carbon dioxide the shock size is larger, such that the g-values are 1.0, 0.95, and 0.72 in these cases. Equation (22) then gives X-ray power outputs of ~15, 30, and ~50 MW, thus being modestly enhanced compared with the values for water.

5. THE SOLAR PROTON FLUX AT 9P/TEMPEL 1

To estimate the solar wind conditions at 9P/Tempel 1, data taken by the SWEPAM instrument aboard the *Advanced Composition Explorer* (*ACE*) spacecraft (McComas et al. 1998) were mapped to the location of the comet. *ACE* is located at L1, ~1 million km sunward of Earth. For the period of interest, we calculated when solar wind measured at *ACE* would arrive at the heliocentric distance, R_h, of the comet, assuming that the measured solar wind velocity remained constant. For each solar wind packet mapped to this distance, we noted the subpacket Carrington longitude on arrival. Solar wind number density measurements were adjusted for the increased distance from the Sun assuming an R_h^{-2} relationship.

For a series of points along the comet's trajectory, we thus acquired for the comet's distance a data set of solar wind velocity and density against Carrington longitude. If one assumes rigid corotation of solar wind features and few solar wind transient structures, as was reasonable during this period of declining solar activity, two points at the same heliographic latitude and heliocentric distance are expected to experience similar solar wind conditions when their Carrington longitudes match. Accordingly, the subcomet Carrington longitude was used to select the mapped solar wind packet most likely to represent the conditions at the comet. The relative positions of Earth, Sun, and comet are shown in Figure 5. We note that the relative positions of *ACE* and the comet around the time of the *DI* collision were coincidentally arranged such that for certain solar wind velocities, corotating solar wind structures arrived at both *ACE* and the comet simultaneously. Figure 6 shows the resulting proton flux estimate at the position of the comet binned in samples of 0.25 days. The light-travel time delays between *Swift*, *ACE*, and the comet have also been taken into account in this plot and subsequent figures although these only amount to a few minutes and are therefore of little consequence. The mean solar wind velocity over the 809 day period shown was 470 km s^{-1} with an rms scatter of 110 km s^{-1}. The difference in heliographic latitude between *ACE* and the comet is shown in Figure 7. At the time of impact the difference is ≈4°, but it increases to ≈10° at the end of the *Swift* observations. Given the relatively small longitudinal, latitudinal, and heliocentric distance separations of Earth/*ACE* and the comet and excluding

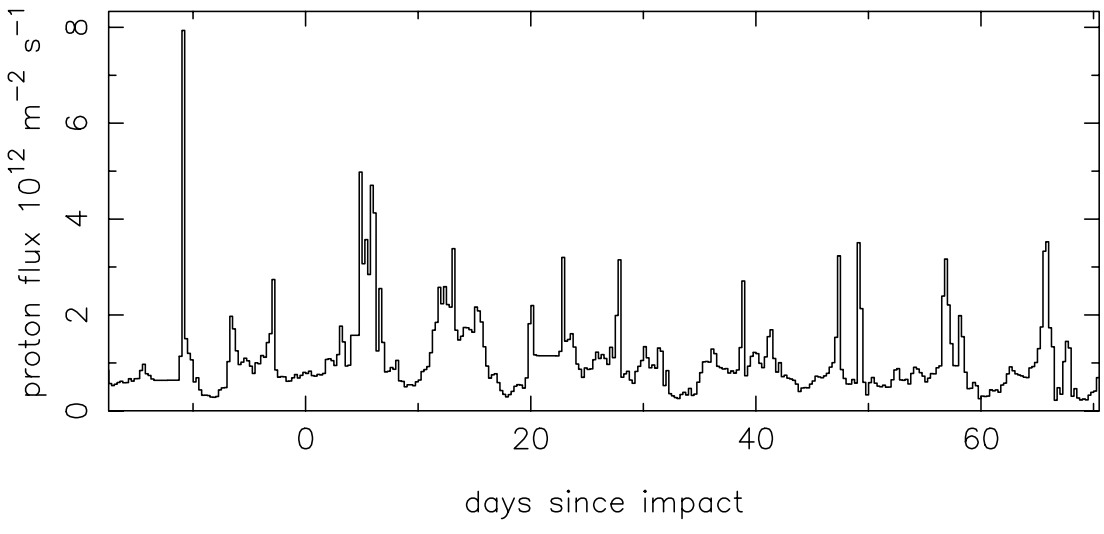

FIG. 6.—Measured solar proton flux from the *ACE* SWEPAM instrument mapped to the position of the comet.

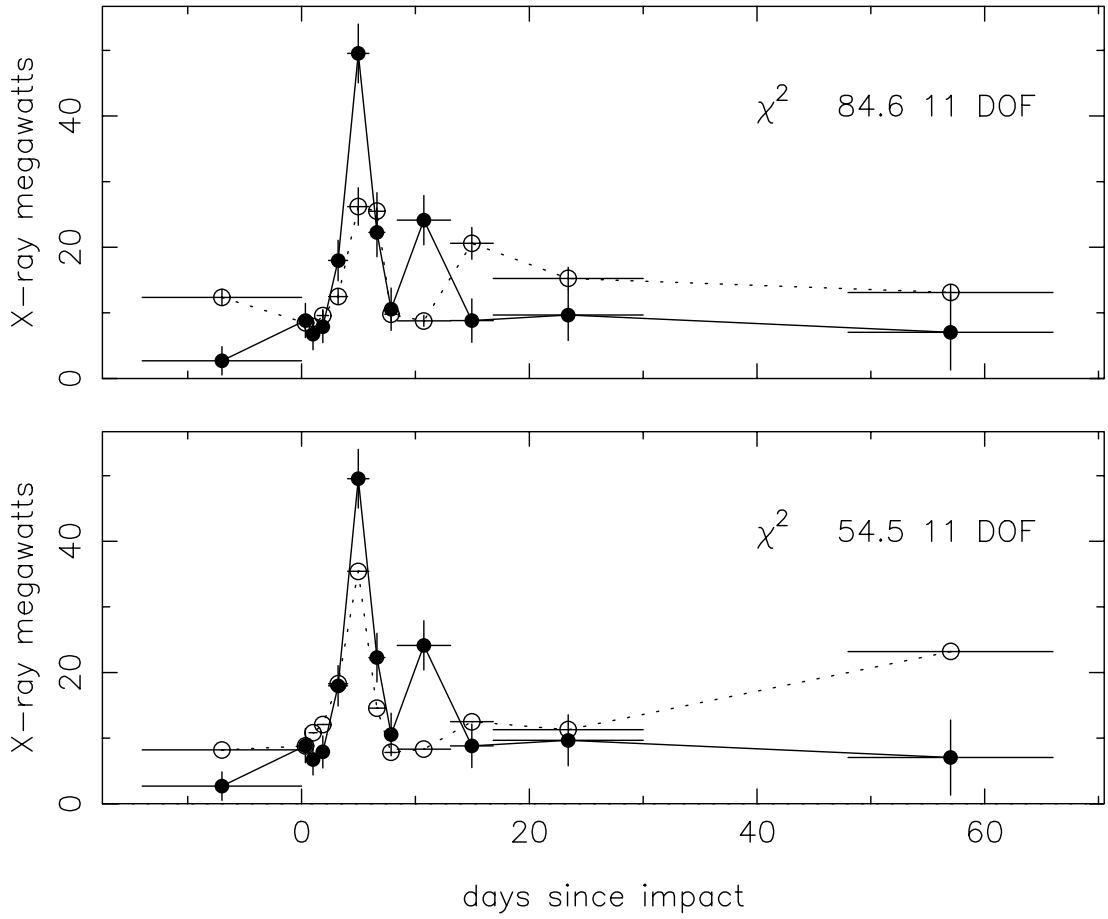

FIG. 8.—Total X-ray power from the comet. *Top:* Measured values (*solid line*) and predicted values (*dotted line*). The proton flux used in the prediction was derived using the nominal time delay between *ACE* and the comet. *Bottom:* Same as top panel, except an extra time slip of −0.75 days was used to produce the minimum χ^2 value between the measurements and prediction.

complications such as transient events, the ballistic mapping of the solar proton flux from *ACE* to the comet is likely to be reliable when considering flux variations and other structure over timescales greater than ≈0.3 days at the time of impact and ≈0.7 days during the later observations.

We can use the spectral fit shown in Figure 4 to convert the X-ray count rates shown in Figure 2 to an X-ray energy flux incident at the *Swift* aperture and then the range shown in Figure 1 to estimate the total soft X-ray power from the comet in the energy band 0.2–1.0 keV assuming that the emission is isotropic. Using equation (21), we can predict the same total X-ray power assuming a constant water production rate Q^* and an estimate of F_p^* obtained by averaging the proton flux shown in Figure 6 over the on-time for each of the X-ray flux data points in Figure 2. The top panel of Figure 8 shows the total measured X-ray power from the comet and the predicted power using $Q^* = 0.57$ and the mapped proton flux. The χ^2 between the measured values and the prediction is 84.6 with 11 degrees of freedom. There are clearly discrepancies between the two; in particular, the peak of the large flare occurs ∼1 day later in the prediction and there is a second enhancement in the prediction at ∼15 days that is not seen in the X-ray measurements. These differences could be due, in part, to systematic errors in the mapping of the *ACE* data. We therefore tried introducing a small time slip into the *ACE* mapping and searched for a value that gave the minimum χ^2 value. The best fit was found for a delay of −0.75 days, which gave $\chi^2 = 54.5$ with 11 degrees of freedom. The measured data and prediction using this time slip and $Q^* = 0.62$ are shown in the bottom panel of Figure 8. In this prediction the position and shape of the main flare match rather well and there is now no second enhancement at ∼15 days.

The introduction of this small time shift clearly improves the match between the measurement and prediction. There are several possible explanations for a timing error in the mapping. As the heliolatitudinal difference between the positions of the comet and *ACE* was nonzero, the three-dimensional nature of the corotating interaction regions being encountered in the solar wind could impart a small shift, particularly toward the end of the period when the latitudinal separation was at its greatest. The heliospheric current sheet at this time was, however, quite highly inclined to the solar equator, making a difference as large as −0.75 days unlikely. Stream-stream interactions, as fast wind continued to impact slower wind traveling ahead of it as it traversed the ∼0.5 AU radial distance from *ACE* to the comet, may have introduced small differences between the *ACE* and comet solar wind conditions that were not covered by the ballistic mapping applied here.

The influence of interplanetary coronal mass ejections (ICMEs) and possibly also solar flares is a potentially major complication to determining the solar wind conditions at the comet. ICMEs are limited in longitudinal and latitudinal extent and therefore may have reached *ACE* or the comet without being detected at the other location. Such events often involve a doubling of solar wind speed (Gosling 1997), field strength increases, and up to a factor of 30 increase in particle number density (Burlaga et al. 1998). As the two X-ray flux enhancements occurred within ∼11 days post-impact, we concentrate on July 1–15 inclusive, the period during

which CMEs erupted that could have affected the comet within that 11 day window. The *Solar and Heliospheric Observatory* (*SOHO*) LASCO CME catalog[12] (Yashiro et al. 2004) lists 66 observed eruptions during July 1–15. Only a fraction of these would have been directed toward the comet, and it is likely that only a small number of this subgroup could have been significant enough to cause major changes to the near-comet solar wind conditions.

The relatively small $\sim 33^\circ$ longitudinal separation of Earth and the comet made the identification of comet-directed CMEs straightforward. Seen from Earth, seven CMEs were partial or full halo events originating on the Sun's near side: one on July 5, three on July 7, one on July 9, plus two west limb eruptions on July 13 and 14. The latter pair could have reached the comet but would have passed Earth first. The July 5 event first detected by LASCO at 15:30 UT had a plane-of-sky speed of 772–832 km s^{-1}. If this approximates the true three-dimensional velocity range, arrival at 9P/Tempel 1 was probably during July 8.8–9.0, i.e., 4.55–4.75 days postimpact, agreeing well with the X-ray flux peak ~ 5 days postimpact. As ICMEs often decelerate, arrival may have been later. The CME originated only 15° from the July 9 subcomet location, implying a very high likelihood of interaction with the comet. Indeed, this ICME did reach Earth, at $\sim$09:00 UT on July 9 (Space Weather Highlights 2005 July 04–10, SWO PRF 1558, NOAA, 2005 July 12). As the CME would have been faster near the comet and in this case was carrying dense prominence material, the comet probably experienced a higher increase in solar wind dynamic and magnetic pressure at this time than did *ACE*.

The three July 7 events all originated at the same active region, near the disk center as seen from Earth, being first detected by LASCO at 11:50, 13:26, and 17:06 UT. The mean of their velocities was 568 km s^{-1}, implying arrival at 9P/Tempel 1 at $\sim$July 12.16, i.e., ~ 7.9 days postimpact. The 1540 km s^{-1} July 9 event, at 22:30 UT, would have reached the comet at $\sim$July 11.6, i.e., ~ 7.4 days postimpact. Also on July 9 was a $\sim$400 km s^{-1}, nonhalo eruption that would have reached the comet at 10.3–12.6 days postimpact. The possibility exists that the slightly westward-directed CME of 22:03 UT July 9 could have interacted with the Earth-directed July 7 ICMEs, probably producing a complex of four ICMEs arriving together at the comet, toward the latter half of the period 6.8–7.9 days postimpact. The uncertainties in the CME propagation directions, physical widths, and absolute velocities make a precise determination of the interplanetary conditions local to the comet impossible. However, it is clear that several solar eruptions could well have disrupted the quiescent, steady, corotating stream regions that dominated most of the observation period, thus perturbing the ballistic *ACE* data mapping employed here.

Discrepancies between the predicted and actual cometary X-ray flux could also result from solar wind composition changes: minor ion composition changes influence the X-ray spectral shape (Schwadron & Cravens 2000). In mapping SWEPAM data, the fractional abundance of solar wind heavy ions, i.e., term α in equation (2), was assumed to be near constant. However, the abundances, composition, and charge states of minor ions can change. Such variations can be seen in the ambient solar wind but are most dramatic within ICME-related solar wind where, e.g., Fe/H ratios can reach a factor of 4–5 that of the ambient solar wind (e.g., Galvin 1997).

Composition variations in the mapped ambient solar wind were addressed by ballistic mapping of minor ion elemental and charge state composition from the *ACE* SWICS/SWIMS instruments (Raines et al. 2005). Significant composition changes were observed, with minor ion number density increases not being entirely in step with solar wind proton fluxes. However, these fluctuations did not readily explain the mismatch between expected and observed cometary X-ray fluxes. For the ~ 5 day postimpact cometary flare, the minor ion abundance increase actually occurred almost 1 day after the proton flux increase, i.e., providing a worse match to the X-ray data than did the SWEPAM proton data alone.

We note that a substantial solar energetic proton flare detected by the *Geostationary Operational Environmental Satellite* (*GOES*) began ~ 3 days after impact and reached a peak at ~ 6 days. This corresponds closely with the peak in cometary X-ray flux observed ~ 5 days after impact, but it is not clear how such relativistic particles would stimulate X-ray emission. The scattering of solar X-rays by very small dust grains (Wickramasinghe & Hoyle 1996) has been found to be insignificant (Lisse et al. 1999; Neugebauer et al. 2000) largely because the required scattering angles are very large and the scattering cross sections of small grains are very low, but very small dust grains were detected from the *DI* collision (Lisse et al. 2006[13]), so we did search for correlations between cometary and solar X-ray fluxes, the latter measured by *GOES-12*. Two M-class solar flares observable from the comet occurred on July 7 and 9, i.e., ~ 3.5 and ~ 5.5 days postimpact, but given the lack of observational or theoretical support for any link between the solar X-ray flux and cometary X-ray emission, we did not pursue it further.

6. THE MOLECULE PRODUCTION RATE FROM 9P/TEMPEL 1

The introduction of the time slip makes only a small difference to the estimate of the assumed constant water production rate, and even after adjustment in the mapping of the *ACE* data there are significant differences between the measured X-ray power and the predicted power using equation (21). The measured power before impact and after 12 days postimpact is significantly less than the prediction, and over the period 0–12 days it is significantly greater. We can use equation (21) to estimate the water production rate using each X-ray power data point and the mapped *ACE* proton flux data. Because the geometric factor g depends on the ratio of the beam radius to the shock radius (R/R_{ss}), a simple iteration was used to find values of Q^* consistent with equations (15), (18), and (21). Figure 9 shows the resulting water production rate as a function of time. Immediately after impact the rate has increased, and it continues to increase for ~ 10 days. The production rate remains elevated for 12 days after impact. We cannot be sure that the rate at later times fell to the preimpact level because of the limited statistics of the observations made in quiescence, but it is consistent with this.

The bottom panel of Figure 9 shows the corresponding estimate of shock distance derived using equation (12). The dotted line shows the radius corresponding to the beam size used to collect the X-ray light curve. This increases with time because the comet is moving away from Earth. At quiescent emission levels the predicted shock radius is smaller than the beam and $g = 1$, but at the peak of the flare postimpact the prediction is somewhat larger than the beam. The smallest geometric factor was at the peak of the flare, $g = 0.95$, so the adjustment to the predictions afforded by including this factor was modest. Table 2 provides a complete listing of the component factors in the calculation of the water production rate.

[12] See http://cdaw.gsfc.nasa.gov/CME_list/.

[13] See http://www.lpi.usra.edu/meetings/lpsc2006/pdf/1960.pdf.

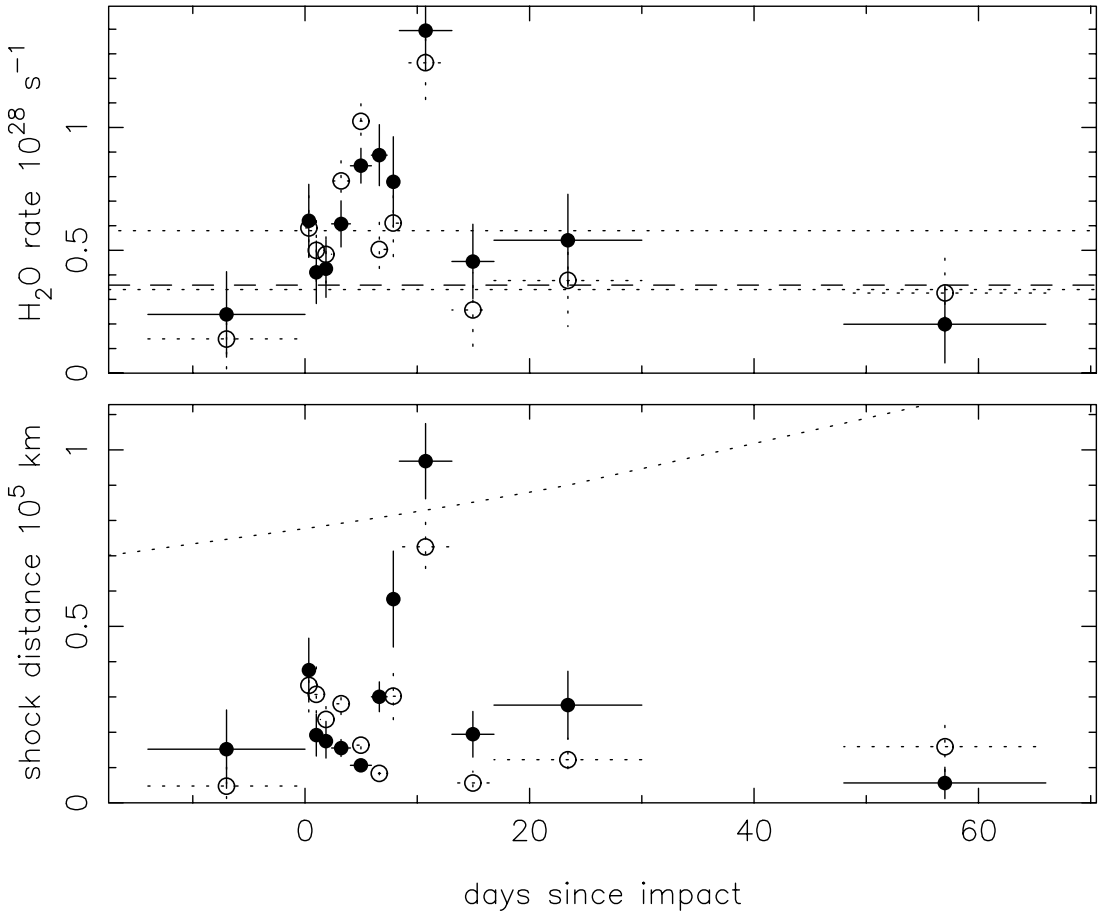

FIG. 9.—*Top:* Estimated water production rate vs. time since impact. The horizontal dashed line is the quiescent level calculated from observations preimpact and >12 days postimpact. The horizontal dotted lines are the preimpact levels calculated by Küppers et al. (2005). The open circles and dotted error bars show the prediction if the nominal proton mapping is used rather than the mapping including the −0.75 day slip. *Bottom:* Subsolar shock radius. The dotted line indicates the beam radius used to generate the X-ray light curve.

The quiescent rate of $\approx 0.36 \times 10^{28}$ s^{-1} corresponds to 0.93×10^7 kg of water per day. Over the 12 day period immediately after impact the increase in X-ray power observed combined with the mapped *ACE* data including a time slip of −0.75 days indicates that the mean rate increased by a factor of 2.37, and if we use the nominal *ACE* mapping, the factor is somewhat larger, 3.55. The total extra water mass shed due to the impact was $(1.9 \pm 0.4) \times 10^8$ kg, a result that is not critically dependent on the accuracy of the *ACE* proton flux mapping employed. If we consider 0–4 days immediately after impact, the extra outgassing rate is considerably lower and the mass of water lost during this period was only $(0.27 \pm 0.09) \times 10^8$ kg.

The results are very similar if we assume that the coma is carbon dioxide dominated rather than water dominated. Using

TABLE 2
SUMMARY OF THE ANALYSIS RESULTS ASSUMING A WATER-DOMINATED COMA

T_{lo} (days)	T_{hi} (days)	N_{exp}	T_{exp} (s)	P_X (MW)	F_p^* (10^{12} m^{-2} s^{-1})	Q^* (10^{28} molecules s^{-1})	R_{ss} (10^5 km)	R^* (10^5 km)	g
−14.0	0.0	19	20790	2.7 ± 2.2	0.71 ± 0.08	0.24 ± 0.17	0.15 ± 0.11	0.75	1.00
0.0.....	0.7	18	20093	8.8 ± 2.6	0.74 ± 0.09	0.62 ± 0.15	0.38 ± 0.09	0.78	1.00
0.7.....	1.4	21	20982	6.7 ± 2.4	0.96 ± 0.11	0.41 ± 0.13	0.19 ± 0.06	0.78	1.00
1.4.....	2.4	22	21497	7.9 ± 2.4	1.09 ± 0.13	0.43 ± 0.12	0.18 ± 0.05	0.79	1.00
2.4.....	4.0	25	21738	18.0 ± 3.1	1.76 ± 0.20	0.61 ± 0.09	0.16 ± 0.02	0.79	1.00
4.0.....	5.9	30	21193	49.5 ± 4.5	3.58 ± 0.42	0.84 ± 0.07	0.11 ± 0.01	0.80	1.00
5.9.....	7.3	20	20308	22.3 ± 3.7	1.33 ± 0.16	0.89 ± 0.12	0.30 ± 0.04	0.81	1.00
7.3.....	8.4	23	20924	10.6 ± 3.2	0.61 ± 0.07	0.78 ± 0.18	0.58 ± 0.14	0.81	1.00
8.4.....	13.1	25	20699	24.1 ± 3.7	0.65 ± 0.08	1.39 ± 0.15	0.97 ± 0.11	0.83	0.95
13.1.....	16.8	19	17405	8.8 ± 3.3	1.05 ± 0.14	0.45 ± 0.15	0.19 ± 0.06	0.85	1.00
16.8.....	30.0	36	18050	9.7 ± 3.9	0.88 ± 0.11	0.54 ± 0.19	0.28 ± 0.10	0.90	1.00
48.0.....	66.0	30	24657	7.0 ± 5.7	1.59 ± 0.17	0.20 ± 0.16	0.06 ± 0.04	1.14	1.00

NOTES.—T_{lo} and T_{hi} are the temporal range of each data period, N_{exp} is the number of exposure slots over this range, and T_{exp} is the total exposure time of these slots. P_X is the X-ray power, F_p^* is the proton flux, Q^* is the H_2O production rate, R_{ss} is the shock radius, R^* is the beam radius, and g is the geometrical beam correction factor.

TABLE 3
SUMMARY OF THE ANALYSIS RESULTS ASSUMING A CARBON DIOXIDE–DOMINATED COMA

T_{lo} (days)	T_{hi} (days)	N_{exp}	T_{exp} (s)	P_X (MW)	F_p^* (10^{12} m^{-2} s^{-1})	Q^* (10^{28} molecules s^{-1})	R_{ss} (10^5 km)	R^* (10^5 km)	g
−14.0	0.0	19	20790	2.7 ± 2.2	0.71 ± 0.08	0.21 ± 0.14	0.35 ± 0.23	0.75	1.00
0.0	0.7	18	20093	8.8 ± 2.6	0.74 ± 0.09	0.50 ± 0.11	0.78 ± 0.17	0.78	1.00
0.7	1.4	21	20982	6.7 ± 2.4	0.96 ± 0.11	0.35 ± 0.10	0.43 ± 0.12	0.78	1.00
1.4	2.4	22	21497	7.9 ± 2.4	1.09 ± 0.13	0.37 ± 0.09	0.39 ± 0.10	0.79	1.00
2.4	4.0	25	21738	18.0 ± 3.1	1.76 ± 0.20	0.53 ± 0.07	0.35 ± 0.05	0.79	1.00
4.0	5.9	30	21193	49.5 ± 4.5	3.58 ± 0.42	0.76 ± 0.06	0.25 ± 0.02	0.80	1.00
5.9	7.3	20	20308	22.3 ± 3.7	1.33 ± 0.16	0.73 ± 0.09	0.64 ± 0.08	0.81	1.00
7.3	8.4	23	20924	10.6 ± 3.2	0.61 ± 0.07	0.64 ± 0.14	1.23 ± 0.26	0.81	0.81
8.4	13.1	25	20699	24.1 ± 3.7	0.65 ± 0.08	1.26 ± 0.13	2.28 ± 0.24	0.83	0.50
13.1	16.8	19	17405	8.8 ± 3.3	1.05 ± 0.14	0.39 ± 0.12	0.44 ± 0.13	0.85	1.00
16.8	30.0	36	18050	9.7 ± 3.9	0.88 ± 0.11	0.45 ± 0.14	0.60 ± 0.19	0.90	1.00
48.0	66.0	30	24657	7.0 ± 5.7	1.59 ± 0.17	0.19 ± 0.15	0.14 ± 0.11	1.14	1.00

NOTE.—Symbols are as for Table 2, except that Q^* is the CO_2 production rate.

equations (19), (20), and (22), we derived the results given in Table 3. The quiescent production rate for carbon dioxide lies in the range $(0.25–0.31) \times 10^{28}$ s^{-1} equivalent to $(1.6–2.0) \times 10^7$ kg per day. The total extra carbon dioxide shed over 12 days has a mass of $(3.9 \pm 0.5) \times 10^8$ kg, and $(0.53 \pm 0.15) \times 10^8$ kg were lost in the period 0–4 days after impact. Note that the masses are larger in this case because the molecular weight of CO_2 is 44 rather than 18 for H_2O.

We can conclude that the impact enhanced the molecule production rate by a significant factor and the total extra mass shed by the comet was in the range $(0.5–4.1) \times 10^8$ kg depending on the composition of the material. Most of this material was lost in the period 4–12 days postimpact rather than immediately after the collision.

7. DISCUSSION

The cause of cometary outbursts is not known. It may be that some if not all of the short optical outbursts seen from comets are triggered by the impact of meteorites, but the evidence from observations of *DI* suggests otherwise (Küppers et al. 2005). Given the X-ray production mechanism discussed above, X-ray outbursts from comets could be triggered by an increase in the solar wind and/or the water production rate. The analysis above indicates that the *Swift* XRT observations exhibit X-ray flaring through both of these possibilities. The X-ray light curve (Figs. 2 and 8) exhibits a double peak structure, but this is not mirrored at a significant level in the molecule production rate shown in Figure 9. This double structure is a consequence of the peaks in the solar wind flux at ~5 and ~13 days, which can be seen in Figure 6.

The preimpact water production levels calculated by Küppers et al. (2005) are in excellent agreement with the quiescent level estimated from the *Swift* X-ray data. These levels are shown in Figure 9. Barring a coincidental transient solar wind event that was not included in our estimate of the solar wind flux, F_p^*, the extended X-ray flare was, in part, caused by an increase in the molecule production rate Q^*. The enhanced postimpact production rate deduced from the X-ray observations peaks ~5 days after impact and persists longer than other phenomena associated with impact seen in UV/optical/IR/radio. The ground-based measurements of OH by Schleicher et al. (2006) continued for 5 days after impact, and they show the OH returning to ambient within about 5 days, which is inconsistent with the molecule production rate derived here if it is due to water.

The total water mass liberated is a factor of 42 larger than estimated from observations of OH at 308 nm (Küppers et al. 2005). However, these observations only cover the first 40 hr period after impact and therefore are only sensitive to the immediate production of gaseous water by *DI* in a small volume surrounding the nucleus. The observed X-ray power indicates that the extra outgassing was modest over the period 0–4 days and the water liberated during this period was only a factor of 6 larger than that estimated from the OH measurements.

The underlying assumption used in the prediction from the optical observations is that OH is produced by the dissociation of water molecules that are flowing from the comet. Under normal conditions this flow is generated by sublimation from the surface. If the outflow speed is ~1 km s^{-1}, then the material passes through the XRT field of view in ~1 day. Thus, to explain the X-ray results, we require an extra source of water or similar volatiles at or near the comet that lasts for the duration of the X-ray flare. It could be that either this water was produced from the surface several days after impact or the impact liberated the water as slow moving ice grains ($\ll$1 km s^{-1}) rather than gas. Ice grains with sizes in the range 1–10 μm were observed in the ejecta of the impact (Sunshine et al. 2006a), but the lifetimes of grains this size are only a few hours (Patashnick & Rupprecht 1977).

The extra source of volatiles could be lying on the surface of the comet. Exposed areas of water ice deposits were detected on the surface of 9P/Tempel 1 postimpact (Sunshine et al. 2006b), but the total area seen was less than required to support the ambient outgassing from the comet. Similar areas of other volatiles including carbon dioxide may have been exposed by the impact producing a temporary increase in the molecular outgassing rate. A thin ejecta blanket deposited on the comet surface by the impact to form evaporating "snow banks" would be difficult to see in reflected light but could be responsible for a significant increase in the outgassing rate.

The relative strength of emission lines in the X-ray spectrum is expected to generally vary with ambient solar wind speed. Calculations by Lisse et al. (2005) indicate that low speeds of 300 km s^{-1} (typically associated with high density near the ecliptic plane) produce lower C line/O line ratios than high speeds of 600 km s^{-1}. Using the line strengths in Table 1, the ratio $(C^{+5} + C^{+6})/(O^{+7} + O^{+8}) = 2.1$, which is very similar to the prediction of Lisse et al. (2005) for a wind speed of 600 km s^{-1}. This speed is somewhat higher than the average at the comet of 438 ± 51 km s^{-1} estimated from the *ACE* data.

It is of course possible that the increase in water and/or carbon dioxide production rate derived from the X-ray data was not associated with the impact, but if this is so, what did cause the increase?

8. CONCLUSIONS

9P/Tempel 1 is a relatively weak/inactive comet both in the optical and adjacent bands and in soft X-rays. We have described a simple theoretical model that can be used to derive the total X-ray power expected from such a comet in terms of the incident solar wind flux and production rate of water or carbon dioxide molecules from the comet. The X-rays are produced by charge exchange between highly charged ions of minor species in solar wind and neutral molecules outgassed from the comet. For weak comets the X-ray production derives from the addition of two terms. The first term is simply the emission expected as the solar wind sweeps through the coma, and the second is a modification/enhancement introduced because a shock is produced on the sunward side of the comet and a compressed region develops downstream from this shock. The soft X-ray surface brightness distribution observed by the *Swift* XRT has a smooth symmetric profile that falls as $\sim 1/r$ and has an FWHM of 1.03×10^5 km in full agreement with the expectations of the model. The observed spectrum exhibits line blend features that can be identified as the expected emission from $C^{+5/+6}$, $O^{+7/+8}$, and Ne^{+9} ions in the solar wind. The quiescent X-ray power (not including the 12 days immediately after *DI* impact) can be used to derive a water production rate that is in excellent agreement with estimates made from optical and UV measurements.

Applying the model over the period 0–12 days after impact shows that an enhanced water and/or carbon dioxide production rate, a factor of $\sim$2.5 greater than the quiescent level, was responsible for an extended soft X-ray outburst from the comet. If this outburst was caused by the *DI* impact, water ice or other volatiles must have been exposed at the surface by the collision or initially shed as small grains rather than neutral gas. The exposed surface and/or the grains then sublimed over a period of 12 days.

We would like to thank Antonino Cucchiara, Claudio Pagani, Judy Racusin, David Morris, Scott Koch, and Pete Roming at the *Swift* Mission Operations Center for all of their help in scheduling and running the 9P/Tempel 1 *Swift* observation campaign. We are indebted to the *ACE* SWEPAM and SWIMS/SWICS instrument teams and the *ACE* Science Center for providing the solar wind data, and we thank Carey Lisse for useful discussions about the interpretation of the X-ray data from comets and 9P/Tempel 1 in particular. We acknowledge the use of information from the Space Environment Center, Boulder, CO, National Oceanic and Atmospheric Administration (NOAA), US Department of Commerce. G. H. J. was partially supported by the Max-Planck Society. J. O. acknowledges support from PPARC. The *SOHO* CME catalog is generated and maintained at the CDAW Data Center by NASA and the Catholic University of America in cooperation with the Naval Research Laboratory. *SOHO* is a project of international cooperation between ESA and NASA.

REFERENCES

A'Hearn, M. F., et al. 2005, Science, 310, 258
Arnaud, K. 1996, in ASP Conf. Ser. 101, Astronomical Data Analysis Software and Systems, ed. G. Jacoby & J. Barnes (San Francisco: ASP), 17
Belton, M. J. S., et al. 2005, Space Sci. Rev., 117, 137
Burlaga, L., et al. 1998, J. Geophys. Res., 103, 277
Burrows, D. N., et al. 2005, Space Sci. Rev., 120, 165
Cravens, T. E. 1997, Geophys. Res. Lett., 24, 105
———. 2002, Science, 296, 1042
Cravens, T. E., & Gombosi, T. I. 2004, Adv. Space Res., 33, 1968
Galeev, A. A., Cravens, T. E., & Gombosi, T. I. 1985, ApJ, 289, 807
Galvin, A. B. 1997, in Coronal Mass Ejections, ed. N. Crooker, J. A. Joselyn, & J. Feynmann (Geophys. Monogr. 99; Washington, DC: AGU), 253
Gehrels, N., et al. 2004, ApJ, 611, 1005
Gosling, J. T. 1997, in Coronal Mass Ejections, ed. N. Crooker, J. A. Joselyn, & J. Feynmann (Geophys. Monogr. 99; Washington, DC: AGU), 9
Häberli, R. M., Gombosi, T. I., De Zeeuw, D. L., Combi, M. R., & Powell, K. G. 1997, Science, 276, 939
Huebner, W. F., Keady, J. J., & Lyon, S. P. 1992, Ap&SS, 195, 1
Krasnopolsky, V. 1997, Icarus, 128, 368
Küppers, M., et al. 2005, Nature, 437, 987
Lisse, C. M., et al. 1996, Science, 274, 205
———. 1999, Icarus, 141, 316
———. 2005, ApJ, 635, 1329
———. 2006, *Spitzer Space Telescope* Observations of the Nucleus and Dust of *Deep Impact* Target Comet 9P/Tempel 1, Abstract 1960, Lunar and Planetary Science Meeting XXXVII
McComas, D. J., Bame, S. J., Barker, P., Feldman, W. C., Phillips, J. L., & Riley, P. 1998, Space Sci. Rev., 86, 563
Meech, K., et al. 2005, Science, 310, 265
Neugebauer, M., et al. 2000, J. Geophys. Res., 105, 20949
Patashnick, H., & Rupprecht, G. 1977, Icarus, 30, 402
Raines, J., Lepri, S. T., Zurbuchen, T. H., Gloeckler, G., & Fisk, L. A. 2005, in *Solar Wind 11/SOHO 16*—Connecting the Sun and Heliosphere, ed. B. Fleck & T. H. Zurbuchen (ESA SP-592; Noordwijk: ESA), 101
Richardson, J. E., & Melosh, H. J. 2006, Modeling the Ballistic Behavior of Solid Ejecta from the *Deep Impact* Cratering Event, Abstract 1836, Lunar and Planetary Science Meeting XXXVII
Schleicher, D., & Barnes, K. 2005, IAU Circ., 8546, 1
Schleicher, D. G., Barnes, K. L., & Baugh, N. F. 2006, AJ, 131, 1130
Schwadron, N. A., & Cravens, T. E. 2000, ApJ, 544, 558
Sunshine, J. M., et al. 2006a, 37th Lunar and Planetary Science Conference, Abstract 1890
———. 2006b, Science, 311, 1453
Wegmann, R., & Dennerl, K. 2005, A&A, 430, L33
Wegmann, R., Dennerl, K., & Lisse, C. M. 2004, A&A, 428, 647
Wegmann, R., Schmidt, H. U., Lisse, C. M., Dennerl, K., & Englhauser, J. 1998, Planet. Space Sci., 46, 603
Wickramasinghe, N. C., & Hoyle, F. 1996, Ap&SS, 239, 121
Yashiro, S., Gopalswamy, N., Michalek, G., St. Cyr, O. C., Plunkett, S. P., Rich, N. B., & Howard, R. A. 2004, J. Geophys. Res., 109, A07105